Available online at www.sciencedirect.com
ScienceDirect
Trans. Nonferrous Met. Soc. China 35(2025) 3428−3442
Transactions of Nonferrous Metals Society of China
www.tnmsc.cn

Synergistic enhancement of strength and plasticity in CoCrFeNiMn high-entropy alloys by novel core−shell microstructure design

Chong-yang LIU[1,2], Xiao-song JIANG[1,2], Hong-liang SUN[1,2], Zi-xuan WU[3], Liu YANG[4]

1. Key Laboratory of Advanced Technologies of Materials, Ministry of Education, Southwest Jiaotong University, Chengdu 610031, China;
2. School of Materials Science and Engineering, Southwest Jiaotong University, Chengdu 610031, China;
3. School of Engineering and Materials Science, Queen Mary University of London, London E1 4NS, United Kingdom;
4. Institute for Applied Materials (IAM-WK), Karlsruhe Institute of Technology (KIT), Karlsruhe 76131, Germany

Received 22 February 2024; accepted 19 November 2024

Abstract: The novel core−shell SiC@CoCrFeNiMn high-entropy alloy (HEA) matrix composites (SiC@HEA) were successfully prepared via mechanical ball milling and vacuum hot-pressing sintering (VHPS). After sintering, the microstructure was composed of FCC solid solution, $Cr_{23}C_6$ carbide phases, and Mn_2SiO_4 oxy-silicon phase. The relative density, hardness, tensile strength, and elongation of SiC@HEA composites with 1.0 wt.% SiC were 98.5%, HV 358.0, 712.3 MPa, and 36.2%, respectively. The core−shell structure had a significant deflecting effect on the cracks. This effect allowed the composites to effectively maintain the excellent plasticity of the matrix. As a result, the core−shell SiC@HEA composites obtained superior strength and plasticity with multiple mechanisms.

Key words: high-entropy alloy; SiC nanoparticles; microstructure design; core−shell structure; tensile properties; strength and plasticity synergy

1 Introduction

High entropy alloys (HEAs) are novel alloys composed of multiple major alloying elements [1]. CANTOR et al [2] proposed a multicomponent CoCrFeMnNi alloy (named Cantor alloy) with iso-atomic ratio. Cantor alloys are one of the most researched and promising HEAs [3,4]. Ordered phases and intermetallic phases are present in HEAs [5], as well as more complex eutectic mixtures or solid solutions with disordered structures [6,7]. Cantor alloys have a typical FCC phase structure with relatively low yield strength and excellent strain-hardening properties under both room and low temperature conditions, thus maintaining excellent toughness [8−11].

SiC nanoparticles can effectively improve the strength, hardness, wear resistance and other multiple properties of composites by virtue of fine grain strengthening, Orowan rings, thermal expansion coefficient, and solid solution strengthening, etc [12]. COLOMBINI et al [13] and ROGAL et al [14] indicated that SiC nanoparticles were effective in increasing the hardness and yield stress of CoCrFeMnNi HEA. SiC decomposes and reacts at high temperatures to form carbides and oxides, and these second phase particles increase the strength of the HEA [13]. LI et al [15] showed that the in-situ reaction between SiC particles and matrix alloys during sintering can significantly increase the microhardness of composites. Especially when Cr is present in the HEA, SiC decomposes and reacts with Cr to produce the more

Corresponding author: Xiao-song JIANG, Tel: +86-28-87634177, E-mail: xsjiang@swjtu.edu.cn
https://doi.org/10.1016/S1003-6326(25)66890-7

stable carbide Cr_7C_3 or $Cr_{23}C_6$. However, while SiC particle reinforced composites are effective in increasing the strength, the plasticity is greatly affected [16]. Balancing strength and plasticity have always been a long-standing problem for metal matrix composites. In recent years, solving this problem by constructing heterogeneous structures has become a new research strategy [17,18].

Currently, several heterogeneous structures with significantly enhanced strength and plasticity have been successfully constructed, such as core−shell, laminate, gradient and bionic structures [17,19]. Heterogeneous structures achieve superior strength−conductivity synergistic properties through the interaction of multiple strengthening mechanisms [20]. For example, strain localization is suppressed, dislocation glide is hindered, stress concentration is avoided and cracks are blunted, flexed and branched [19,21,22]. GUO et al [23] have prepared Ti−Al_3Ti core−shell structure by in-situ reaction of Al matrix and Ti matrix. MA et al [24] fabricated the core−shell structure of Al matrix with Al_3Ni−NiAl , which was found to have a wavy crack extension path. The results showed that the composite has high strength and ductility. SUN et al [25] succeeded in constituting Hadfield steel with the nanocrystalline−amorphous core−shell structure by laser fusion cladding. LIU et al [26] synthesized SiC nanoparticles reinforced magnesium-matrix composites with heterogeneous core−shell structure by mechanical ball milling. The core−shell structure achieved a balance between superior strength and plasticity by impeding crack expansion, transferring load-bearing capacity, and alleviating stress concentrations. In the core−shell structure, the matrix as a soft phase contributes to the excellent plasticity of the alloy, while the hard particles in the shell are essential for increasing the strength. High entropy alloys, as novel high-strength alloys, are inevitably the first choice for hard particles in core−shell structures. Mechanical ball milling can improve the strength and plasticity of high entropy alloys, which is common in industry. This is certainly an efficient and appropriate development strategy.

In this study, a core−shell structure was constructed in the high-entropy alloy by mechanical ball milling. The microstructure, phase composition and fracture morphology of the composites were studied and analyzed. The strengthening and toughening mechanisms of the SiC@HEA composites were further analyzed. The core−shell structure studied in this work has special structural properties and unique mechanical properties. The microstructural design of the core−shell structure was studied and analyzed, and its mechanical properties were tested. This work provides some theoretical guidance for the development of high-entropy alloys.

2 Experimental

2.1 Raw materials and sample fabrication

The raw material powders were iso-atomic CoCrFeNiMn HEA pre-alloyed powders (particle size of 45−105 μm), and SiC nanoparticles (particle size of 20−50 nm). SiC powders (0.5, 1.0, and 1.5 wt.%) were mixed with HEA powders through mechanical ball milling in a tungsten carbide jar. Tert-butyl alcohol (TBA) was used as a protective medium during ball milling. The mass ratio of balls to composites was 20∶1 at 240 r/min for 4 h. Afterwards, the composites were dried in a freeze drier for 24 h to adequately remove the TBA. The powder mixture was sintered in a VHPS furnace at 1000 °C for 1 h. The heating rate was 10 °C/min and the pressure was gradually increased to 30 MPa during the heating process. The maximum pressure was reached at the highest temperature and remained constant during the holding process. After the holding process, the samples were cooled in the furnace. The fabrication process of the SiC@HEA matrix composites is shown in Fig. 1.

2.2 Characterization and mechanical performance tests of composites

After sintering, the composite was cut into small bulks by wire cutting. These bulks were sanded with silicon carbide sandpaper and then polished until without visible scratches. To characterize the microstructure of the SiC@HEA after polishing, the phase composition was analyzed by X-ray diffraction (XRD, Rigaku Ultma IV), with 2θ ranging from 10° to 80° in steps of 0.02°. The microstructure and fracture morphology of the composites were analyzed by scanning electron microscope (SEM, ZEISS Sigma 300). The microstructure of the SiC@HEA matrix composites was determined by transmission electron microscopy (TEM, FEI Talos F200X with 200 kV

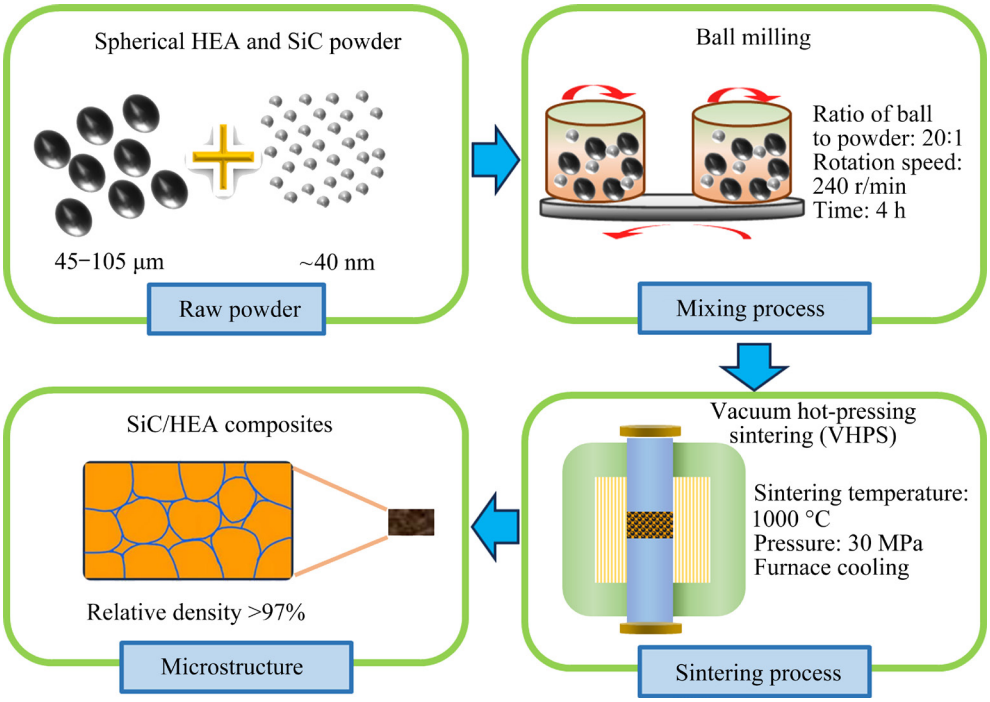

Fig. 1 Preparation process of SiC@HEA composites

accelerating voltage). The specific composition of the second phase was also analyzed by selected area electron diffraction (SAED).

The density of the SiC@HEA was tested based on the drainage method and calculated from the theoretical density of alloy. Mechanical properties were tested by the Vickers hardness machine (HVS−1000Z), by applying a load of 1 kg with an indenter on the mechanically polished surface. The hardness was tested at several random locations in the composite. The average hardness was calculated to minimize errors. Mechanical properties were tested by a universal testing machine (WDW−3100). The tensile specimens were I-beams (test dimensions according to GB 228.1 standard, marking distance of 10 mm, thickness of 2 mm, and width of 4 mm), and each group of specimens was tested four times to minimize the error.

3 Results and discussion

3.1 Morphology of powder

The initial morphology of the HEA powder was spherical. SiC nanoparticles were combined with HEA powder particles by ball milling. In order to obtain the excellent experimental parameters for ball milling, a pre-experiment of planetary ball milling was made (in Fig. 2). Pre-experiments were performed using SiC@HEA powders of 1.0 wt.% SiC, and ball milling at 240 r/min. Figures 2(a−d) show the morphology of the SiC@HEA composite powders for different ball milling time (2−8 h). The HEA powder could collide with SiC particles, alloy jars, alloy balls and other HEA powders. The HEAs powder underwent various processes ranging from initial tiny deformations, through larger deformations during cold welding, to eventual fracture and fragmentation [27]. SiC nanoparticles were gradually impinged into the HEA powder during the ball milling process, which gradually accelerated as the ball milling proceeded. During the ball milling process, the HEA powder underwent plastic deformation, which was gradually intensified, and finally broke up completely. HEA particles were initially spherical, then fragmented into short columns that gradually broke up and thinned out. Based on the morphology of the HEA powders shown in Fig. 2, the final ball milling time was determined to be 4 h. After 4 h, the HEA powders exhibited a more completely spherical morphology, where the SiC nanoparticles could be well encapsulated on the outside of the HEA particles.

Figure 3 shows the elemental distributions of the SiC@HEA composite powder after ball milling. The uniform distribution of metal elements in the

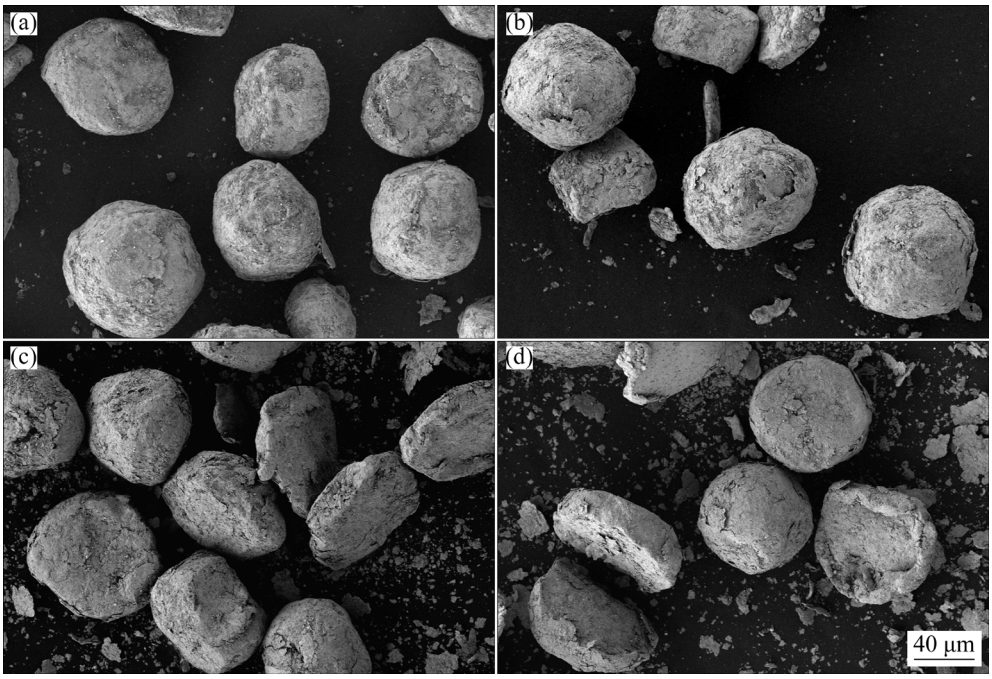

Fig. 2 Morphologies of SiC@HEA composite powders after ball milling for different time: (a) 2 h; (b) 4 h; (c) 6 h; (d) 8 h

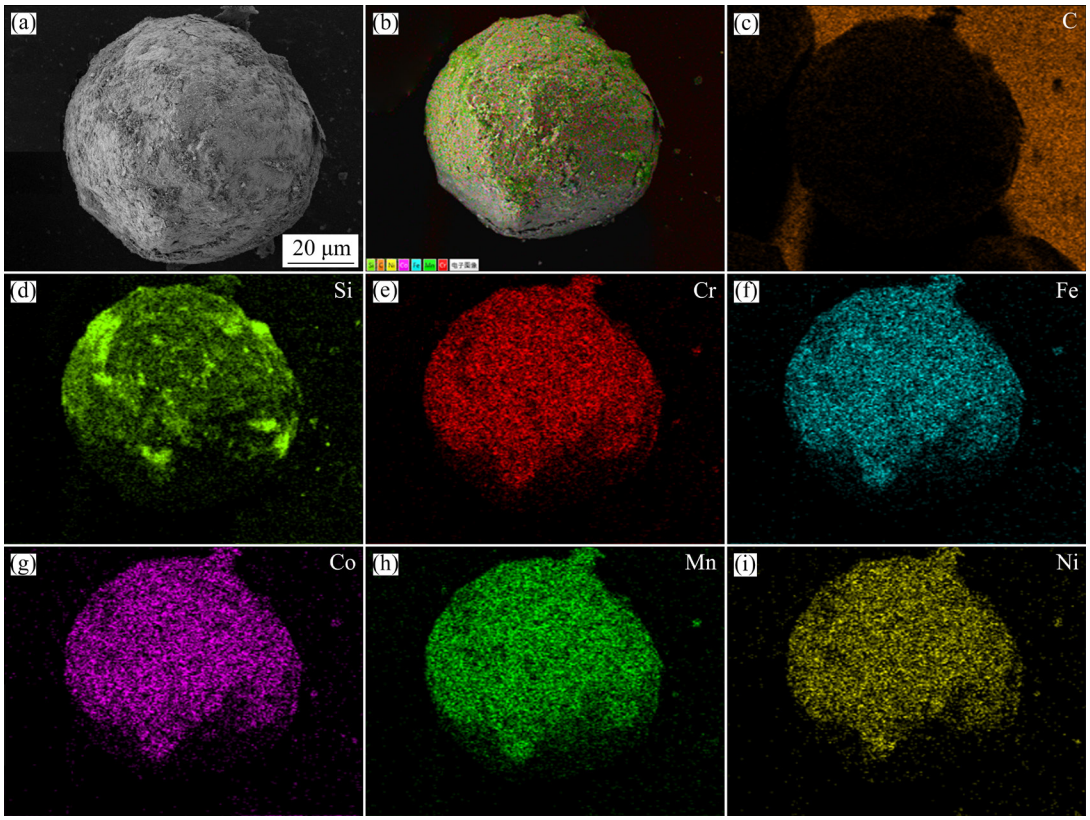

Fig. 3 Elemental distribution images of SiC@HEA composite powders

powders indicated that there was no agglomeration between the HEA powders and SiC nanoparticles. However, Si and C elements were uniformly distributed on the HEA particles, indicating that SiC particles could be completely embedded on the HEA surface. The distribution of the C element was

special, which was caused by the SEM sample preparation. The alloy powder must be immobilized on the conductive adhesive, which is the C-rich region under the EDS, thus creating this special distribution. LUO et al [28] carried out low temperature milling of SiC nanoparticles and magnesium powder. The results showed that ball milling can discrete the harder SiC particles in the softer phase. In the grinding process, the SiC nanoparticles were gradually embedded into the HEA particles due to the impact of the material, forming the core−shell structure. The SiC@HEA powders had an outer layer of SiC nanoparticles incorporated with HEA matrix (hard outer shell) and an inner layer of pure HEA matrix (soft inner core).

3.2 Microstructure of sintered bulk

In order to analyze the composition of the sintered bulk, the SiC@HEA composites were tested by XRD, as shown in Fig. 4. The microstructure of the composite mainly consisted of FCC matrix, and the crystallographic indices of the three main diffraction peaks were (111), (200) and (220), which indicated that the incorporation of the SiC did not affect the structure of the HEA matrix. Furthermore, the diffraction peaks of carbide also appeared in the XRD patterns and were enhanced with the incorporation of SiC nanoparticles. There were two factors for the formation of carbide. On the one hand, the unstable SiC would decompose at high temperatures, while the elements C and Cr would form the more stable carbide Cr_7C_3 or $Cr_{23}C_6$ at high temperatures. The type of carbide mainly depends on the sintering temperature, and the contents of elements C and Cr. SZKLARZ et al [29] and COLOMBINI et al [13] enhanced HEA with different Cr contents by SiC nanoparticles. The results showed that SiC could decompose at high temperatures to form carbides and oxides. On the other hand, the carbides came from the residues of the protective medium during the experimental process, as well as from carbon penetration in the graphite molds during the sintering process. This phenomenon was also found in several other studies [9,30], where the formation of carbide was unavoidable due to the extreme susceptibility of Cr to react with C. PICKERING et al [31] also found some precipitated phase of $M_{23}C_6$ in their long annealing experiments of CoCrFeNiMn. Moreover, the composition of the precipitated phase was similar to that of the precipitated phase around grain boundary in the experiment of HE et al [32]. The results indicated that CoCrFeNiMn HEA generated carbide during the experimental process, which were probably caused by the SiC nanoparticles decomposition or the C-element contamination.

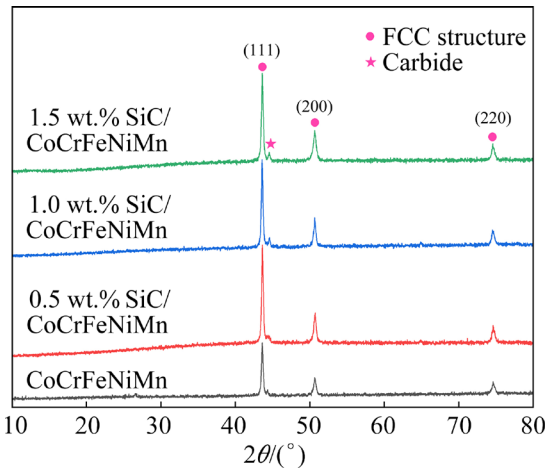

Fig. 4 XRD patterns of SiC@HEA composites

Figure 5 shows the microstructures of the SiC@HEA matrix composites. Figure 5(a) shows the HEA matrix with uniform compositional distribution in the microstructure. Figures 5(b−d) show the composites with SiC content of 0.5, 1.0, 1.5 wt.%, respectively. The microstructure of the composites retained the morphology of the core−shell SiC@HEA powders. The composites were mainly composed of the matrix phase and two precipitated phases. The two precipitated phases were carbide and oxy-silicon phases, as shown in the EDS results. Due to the small size of SiC nanoparticles, as well as the decomposition and reaction at high temperatures, the SiC nanoparticles were not found in Fig. 5. The oxide phase particles were mainly distributed among the HEA particles, which indicated the mixing of external oxygen elements during the powder preparation process. During the experimental process or powder transfer, some of the external air remained on the powder surface and reacted with HEA. The carbide phase was uniformly distributed in the composites and varied with the content of SiC nanoparticles. The results showed that the carbide phase was closely related to the SiC nanoparticles.

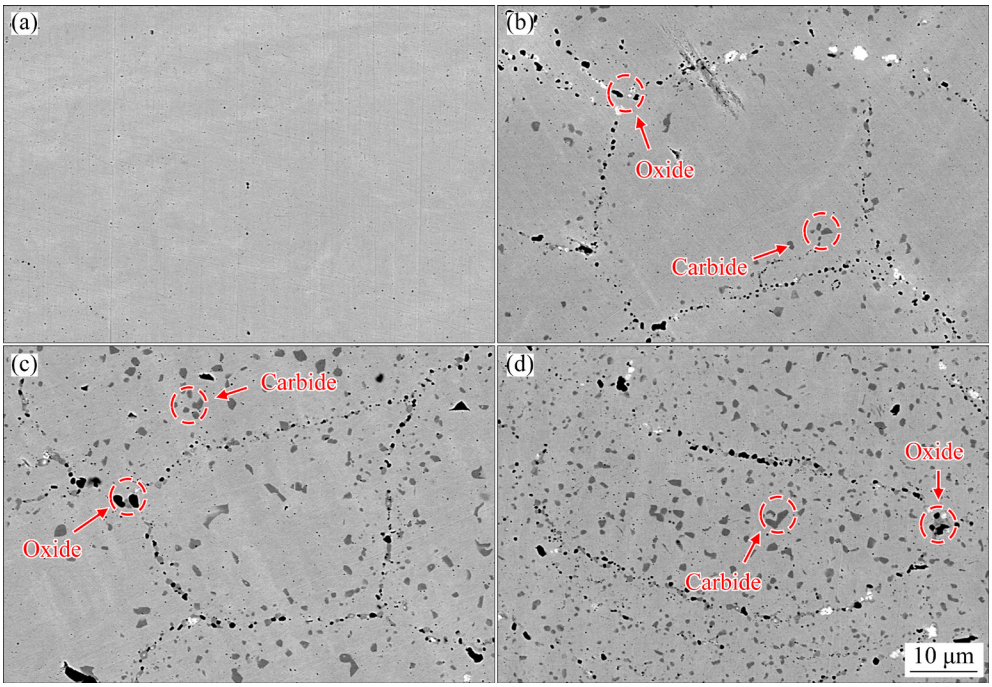

Fig. 5 Cross-sectional SEM images of composites: (a) CoCrFeNiMn; (b) 0.5 wt.% SiC/CoCrFeNiMn; (c) 1.0 wt.% SiC/CoCrFeNiMn; (d) 1.5 wt.% SiC/CoCrFeNiMn

3.3 Microstructure characterized by TEM

To accurately determine the composition of the phases in the microstructure, further probing was carried out by TEM. The results of TEM revealed the microstructure and phase composition of the SiC@HEA composites. Figure 6 shows the element scanning results of the SiC@HEA composite. The elemental distribution confirmed the segregation of Si, C, O, Cr and Mn elements in the composites. The microstructure was dominated by the matrix phase with precipitated carbide phase and oxy-silicon phase at the grain boundary. An unavoidable side effect of mechanical ball milling was the formation of metal oxide. Owing to the extreme binding capacity of the elements Cr, Mn and O in Cantor alloys, it was extremely difficult to avoid oxidation in the mechanical alloying process. Such oxide or carbide particles were also observed in Cantor alloy in some related studies [8,33]. COLOMBINI et al [13] also fabricated FeCoNiCrAl HEA reinforced with SiC nano-particles by powder metallurgical synthesis. It was found that SiC was unstable at high temperatures and more stable carbide and silicide were formed, which would increase the hardness of the alloy. This was comparable to the generation of the second phase in the present work.

In Fig. 7(a), the SiC@HEA composite was composed of the matrix and two different second phases, which were analyzed by SAED, as shown in Figs. 7(c−e). The matrix maintained the FCC structure of the HEA, with the oxy-silicon phase as Mn_2SiO_4 and the carbide phase as $Cr_{23}C_6$. The presence of numerous dislocations and twins could be seen in the microscopic morphology of Fig. 7(a), where the dislocations were entangled and stacked at the diffusive particles. Therefore, these second phase particles were observed to hinder the motion of dislocations. In addition, as shown in Fig. 7(b), some dislocation walls with mesh dislocations existed near the twin crystals. The SAED spectrum of the twin at this location is shown in the lower right corner of Fig. 7(b). There were two reasons why twins appeared. Firstly, during the ball milling process, composite powder underwent substantial plastic deformation and numerous defects were produced. During sintering, deformation from axial loading could lead to the generation of twin crystals. Second, the glide of dislocations was hindered, leading to the formation of regions of high-density dislocations, which also promoted the emergence of the twins [34]. The twin interacted with the dislocations. DENG et al [35] observed numerous dislocations in the microstructure of the fabricated

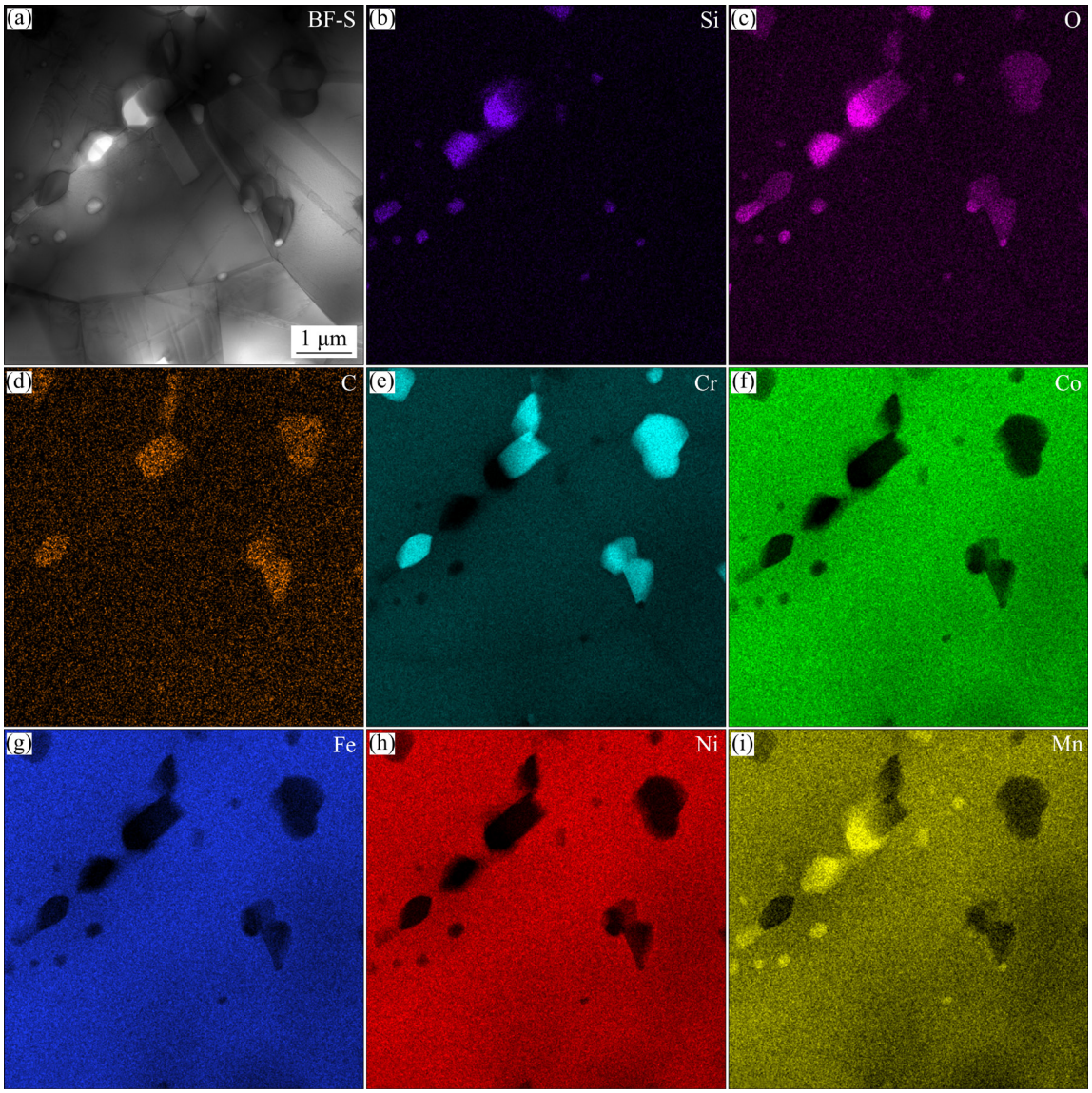

Fig. 6 Elemental distributions in SiC@HEA matrix composites

$Fe_{40}Mn_{40}Co_{10}Cr_{10}$ HEA. These dislocations were stacked on each other and crisscrossed, forming dislocation walls. As these high-density dislocation walls impeded the motion of subsequent dislocations, HEA was simultaneously enhanced by this dislocation reinforcement.

Figure 8 shows the high resolution transmission electron microscope (HRTEM) images of the two second phases with the matrix and their corresponding fast Fourier transform (FFT) images. Figure 8(a) shows the HRTEM image of the carbide phase $Cr_{23}C_6$ and the matrix, where no new compounds were generated at the interface. At the atomic level, $Cr_{23}C_6$ is tightly bound to the matrix interface. The crystal plane of $Cr_{23}C_6$ was (200) with a lattice spacing of 0.556 nm. The crystal plane of the matrix was (111) with a lattice spacing of 0.207 nm. Figure 8(b) shows the HRTEM image of the Mn_2SiO_4 and the matrix, which was a semi-coherent lattice type of bonding as the oxy-silicon phase was tightly bound to the matrix atoms. The crystal plane of the Mn_2SiO_4 phase was (110) with a lattice spacing of 0.447 nm.

3.4 Mechanical properties

The hardness and density of the SiC@HEA composites are shown in Fig. 9. The density of composites was highly dependent on the porosity of the material, especially when the material was prepared by powder metallurgy. As the sintering temperature gradually increased, the contact surface area between the powders gradually increased, the

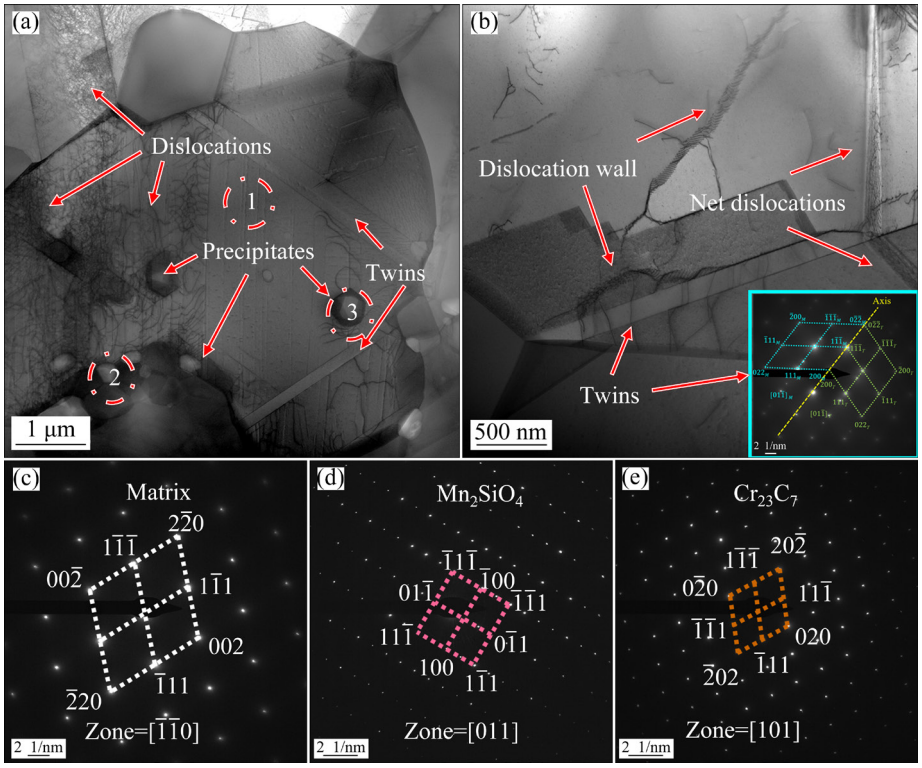

Fig. 7 TEM images of composites: (a, b) Microstructural morphology; (c−e) SAED spectra

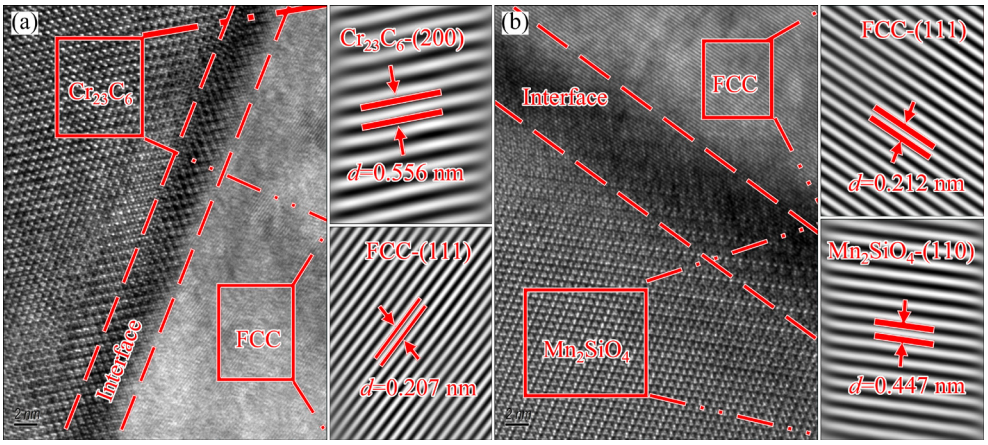

Fig. 8 HRTEM images of second phase and matrix in SiC@HEA composites: (a) $Cr_{23}C_6$ and matrix; (b) Mn_2SiO_4 and matrix

pores gradually contracted until closed, and the alloy eventually became dense. Therefore, density was an important indicator of the success of alloy sintering. Excellent density was an essential index to ensure that the alloy has excellent mechanical properties [36]. The density of the SiC@HEA composites was 97.3%, 98.4%, 98.5%, and 97.7%, corresponding to different SiC nanoparticles contents of 0, 0.5, 1.0, 1.5 wt.%, respectively. Thus, the densities of the SiC@HEA composites all reached a superior level. The composites had a high density due to the fact that they were sintered at high temperatures and held for 1 h.

The hardness of the composites was HV 308.2, HV 334.2, HV 358.0, and HV 363.1, respectively. Hardness is one of the extremely significant mechanical properties of the material. The density of the composites severely affects their hardness. The lower the density of the composite, the more the defects such as voids and micropores were present. The composites all have superior density, so the effect of density on hardness was minor and

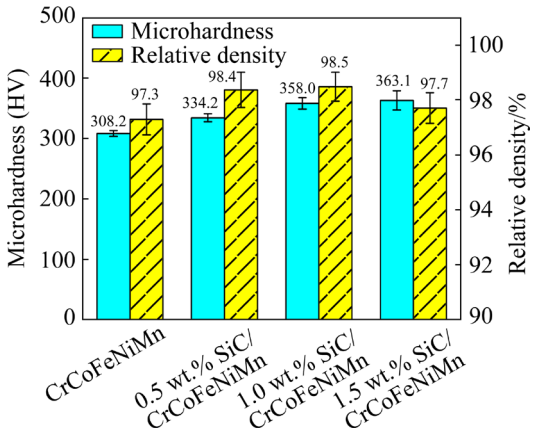

Fig. 9 Hardness and density of SiC@HEA composites

negligible. The change in hardness was mainly due to the incorporation of SiC, which increased the hardness of the composites as the content of SiC nanoparticles increased. The C-element content had a considerable effect on the hardness of the SiC@HEA composites. Carbide generation and solid solution strengthening of the FCC phase by C elements increased the hardness of the HEA matrix.

Figure 10 shows the comparison of tensile stress−strain curves and tensile properties of the SiC@HEA composites. As shown in Fig. 10(a), the tensile strengths of the SiC@HEA composites with 0.5, 1.0, and 1.5 wt.% SiC were 623.9, 712.3, and 611.7 MPa, and elongations were 32.9%, 36.2%, and 29.1%, respectively. The composite with 1.0 wt.% SiC had the highest tensile strength, while the strength of the composite with 1.5 wt.% SiC decreased. This was caused by the increase in SiC content, resulting in an excess of second phase particles. Such particles tended to aggregate and become a source of crack initiation, resulting in reduced strength.

Compared with CoCrFeNiMn HEA, the SiC@HEA composites have higher strength and better deformation capacity. On the one hand, the reinforcement of SiC nanoparticles increased the strength compared to the HEA. The SiC nanoparticles could transfer the loads concentrated on the SiC nanoparticles under external forces. As shown in the shear hysteresis model [43], SiC nanoparticles shared the stresses carried by the HEA matrix, thus effectively increasing the fracture strength of SiC@HEA. In addition, SiC decomposed during the sintering process, generating carbide particles at grain boundaries, producing diffusion strengthening and grain boundary strengthening. When the composite was under external loading, dislocations rapidly sprouted and spread, followed by glide. At this time, due to the “bypassing” of dislocations, the dislocation ring would remain around the hindering particle. This resulted in not only more lattice distortions, but also stronger hindering effect on subsequent dislocations. As a result, SiC nanoparticles and diffuse phase particles enabled dislocation glide to consume more energy, which was favorable to improving the strength and hardness of the SiC@HEA. Several related studies showed that the increase in the fracture strength of the composite is related to the activation of twins in the microstructure [11].

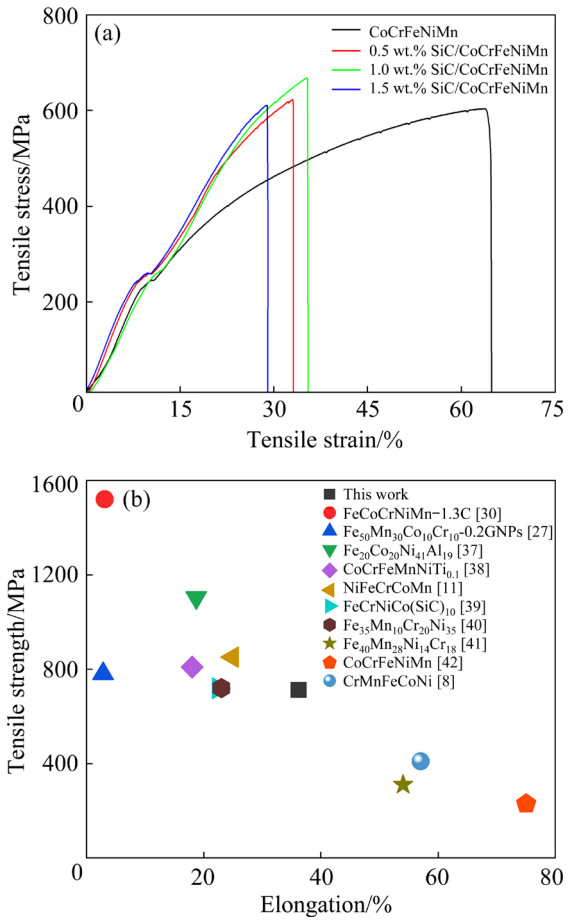

Fig. 10 Tensile test results of SiC@HEA composites: (a) Stress−strain curves; (b) Comparison of tensile properties [8,11,27,30,37−42]

On the other hand, the core−shell structure altered the crack extension path. The deflection of the crack extension increased the energy consumed for fracture. Then, the incorporation of SiC led to the generation of strengthening phases, which

caused additional strengthening mechanisms to further enhance the mechanical properties. As shown in Fig. 10(b), the SiC@HEA composites showed superior synergistic effects of strength and plasticity.

3.5 Fracture behavior

Figure 11 shows the fracture morphology of the SiC@HEA composites after tensile tests. In order to further research the effect of the core−shell structure on the tensile properties, the tensile fracture morphology of the composites was examined. In Figs. 11(a, b), single cracks were distributed along the edge of the spherical particles. In contrast, the SiC@HEA composites with 1.0 wt.% SiC showed a more distinctive core−shell structural morphology, with cracks more distributed along the layer. In Figs. 11(c, d), the fracture morphology of the matrix became flattened. The SiC@HEA composite retained the fracture morphology of the original spherical powder. The results showed that its tensile fracture was also along the core−shell structure.

Figures 11(e, f) show the higher resolution SEM images to further analyze the fracture morphology of composites. Fracture morphology was distributed with numerous dimples, which was the feature of the plastic fracture. During crack extension, the formation and growth of dimples absorbed more energy and contributed to the formation of the ductile features. The size of the dimples in the matrix of the non-core−shell structure was relatively large. Formation and growth of large size dimples consumed more energy during crack propagation. The greater the local resistance of the material to destabilization, the better the plastic toughness [44]. The core−shell structure of the SiC@HEA composites was also distributed with numerous dimples in which the second phase particles were present. The diffusive

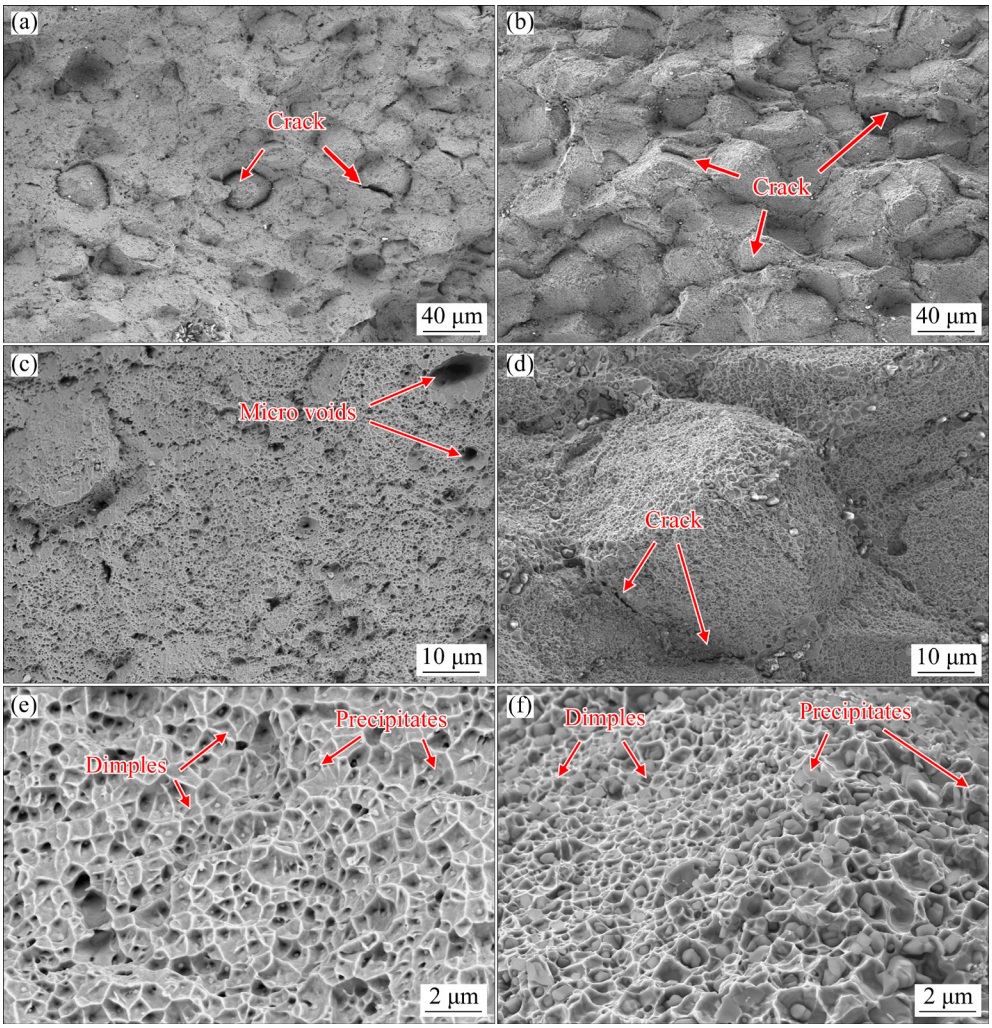

Fig. 11 Fracture morphologies after tensile tests: (a, c, e) Matrix; (b, d, f) SiC@HEA composite with 1.0 wt.% SiC

phase particles had different plasticity from the HEA matrix. Under the applied load, the composite material was deformed, the stress was concentrated on the diffusive phase particles, and microcracks sprouted and spread along the interface. Eventually, dimples were formed at this location and retained in the dimples among the diffusive phase particles.

3.6 Strengthening mechanism

Core−shell SiC@HEA composites achieved superior strength due to multiple strengthening mechanisms (solid solution strengthening, fine grain strengthening, dislocation and twinning strengthening, second phase strengthening, etc). In addition, core−shell SiC@HEA composites maintained excellent plasticity, resulting in an excellent strength− plasticity synergy.

3.6.1 Solid solution strengthening

Solid solution strengthening results from localized stress changes and lattice distortions due to differences in the size of the constituent atoms. Different atomic sizes in composites lead to lattice distortion and solid solution strengthening. This strengthening mechanism can be calculated from the distortion energy of the lattice and the atom concentration [45]:

$$\Delta\sigma_{SS}= AG\varepsilon^{4/3}C^{2/3} \quad (1)$$

where $\Delta\sigma_{SS}$ is the solid solution strengthening value, A is a dimensionless constant depending on composite material, C is the concentration of solid-solution atoms in the composite, G is the shear modulus of the composite, and ε is the lattice distortion induced by solid solution atoms. HEA has multiple major component properties and all atoms can act as solute atoms. As a result, the solid solution strengthening effect is superimposed and enhanced by more solid solubility in HEA [46]. The SiC nanoparticles in core−shell SiC@HEA matrix composites decompose during the sintering process. When the SiC decomposes, the resulting Si and C atoms are much smaller in size than metal atoms. As a result, they exist as interstitial atoms in the microstructure, which leads to lattice distortions in the matrix. For example, C atoms can move into the octahedral interstitials in the HEA matrix lattice (FCC structure), leading to larger lattice distortion energy [47,48].

3.6.2 Fine grain strengthening

The SiC decomposed during the sintering process and generated new phases in-situ at the interface. Diffusive particles and second-phase particles at the interface impede the interfacial extension process. Thus, the growth of the grains was hindered, resulting in the grains becoming remarkably fine [49]. The strengthening of fine grains was mainly caused by the increase of grain boundaries and the avoidance of stress concentration [40]. HEA has excellent thermal stability and slow elemental diffusion effects, resulting in slow crystallization and grain growth to form fine grains. The composition of the HEA matrix composites is more complex than the traditional alloys. However, HEA usually has a stable phase structure. Therefore, the value of fine grain strengthening of the HEA matrix composites can be obtained on the basis of the average grain size, as shown in equation below [45,50]:

$$\Delta\sigma_{HP}= K(d^{-0.5} - d_0^{-0.5}) \quad (2)$$

where $\Delta\sigma_{HP}$ is the fine grain strengthening value, K is the Hall−Petch constant, d and d_0 are the average particle sizes of the composite and HEA matrix, respectively. The SiC nanoparticles hinder the growth of the HEAs grains, leading to more and finer grains. The finer grains allow the HEAs matrix composites to have more fine-grained reinforcement, which contributes to the strength of the composites and maintains their plasticity.

3.6.3 Dislocation and twin strengthening

The TEM image (Fig. 7) showed that numerous dislocations and twins were present in the microstructure of the SiC@HEA composites. The dislocations were hindered at the interface and the second phase particles, and dislocations underwent intercalation, entanglement and accumulation. In addition, the stacked dislocations also hinder the subsequent dislocation movement and plastic deformation of the composites. In the process of mechanical ball milling, severe plastic deformation occurs due to the mutual collision and extrusion between the HEA powder and the alloy balls. Consequently, the higher density of dislocations was produced in HEAs. For HEAs, the diversity of matrix components is different from the thermal expansion coefficient of the reinforcing phase. As temperature changes, the matrix and reinforced phases are deformed to varying degrees, resulting in large localized stresses and numerous dislocations. The value of dislocation reinforcement in HEAs can

be calculated according to Eq. (3) [45]:

$$\Delta\sigma_{Dis}=M\alpha Gb\rho^{1/2} \quad (3)$$

where $\Delta\sigma_{Dis}$ is the dislocation strengthening value in HEAs, M and α are constants related to the material, and the FCC structural material has M and α values of 3.06 and 0.2, respectively. b is the magnitude of Burgers vector, and ρ is the dislocation density. The HEA matrix composites can greatly hinder the dislocation motion due to the characteristics of more grain boundaries, finer grains, and multi-phase composition, resulting in larger dislocation strengthening. Therefore, dislocation and twin strengthening exists in the SiC@HEA composites to obtain superior mechanical properties.

3.6.4 Second phase strengthening

From the elemental distributions (Fig. 6) of the SiC@HEA composites, the microstructure of the composites contains numerous second-phase particles. These particles hinder dislocation glide and lead to entanglement and stacking of the dislocations. Furthermore, according to the morphology of the fractured SiC@HEA composites after the tensile experiments, the second phase particles in the composites affect the fracture process. Due to the different deformability of the second-phase particles and the HEAs matrix, the second-phase particles resulted in indentations. Therefore, the strengthening mechanism of second phase is also included in the SiC@HEA composites. The second phase strengthening is divided into the Orowan and the Ansell−Lenier mechanism. From the fracture morphology, the SiC@HEA composites belong to the Orowan mechanism. The Orowan strengthening of HEA matrix composites is more complex compared to traditional alloys. Therefore, the effects of HEA matrix and reinforcing phase should be considered. Equation (4) for this strengthening value is given below [51]:

$$\Delta\sigma_{Orowan}=\{0.13Gb/d_p[(2f_v)^{-1/3}-1]\}\ln[d_p/(2b)] \quad (4)$$

where $\Delta\sigma_{Orowan}$ is the Orowan strengthening value, and f_v and d_p are the volume fraction and size of the reinforcing phase, respectively. For SiC nanoparticles, the particle size is in the nanometer scale, which possesses a stronger strengthening mechanism under the Orowan mechanism [27]. The diffusive distribution of $Cr_{23}C_6$ carbide and the precipitation distribution of Mn_2SiO_4 oxy-silicon phase at the interface are responsible for the increased yield strength. The glide of dislocations toward these second-phase particles are hindered by entanglement and impede the glide of subsequent dislocations. As a result, the core−shell SiC@HEA composites have high second phase strengthening, which further caused improved mechanical properties.

4 Conclusions

(1) SiC nanoparticles were embedded in the exterior of HEA particles through mechanical ball milling to form the core−shell SiC@HEA powder. After VHPS, SiC decomposed and reacted to form in-situ new diffusive phase around the interface. The microstructure of the SiC@HEA composites consisted of FCC solid solution, $Cr_{23}C_6$ carbide phase and Mn_2SiO_4 oxy-silicon phase.

(2) The density and hardness of the SiC@HEA with 1.0 wt.% SiC were 98.5% and HV 358.0, respectively. Meanwhile, the SiC@HEA composites obtained superior strength and maintained excellent plasticity with tensile strength of 712.3 MPa and elongation of 36.2%.

(3) The core−shell structure of the SiC@HEA composites resulted in superior mechanical properties by multiple mechanisms, which achieved the synergy effect of strength and plasticity. Furthermore, the core−shell structure had an obvious deflection effect on cracks, which allowed the SiC@HEA composites to maintain the excellent plasticity of the HEA matrix.

CRediT authorship contribution statement

Chong-yang LIU: Formal analysis, Writing − Original draft; **Xiao-song JIANG:** Supervision, Project administration, Funding acquisition; **Hong-liang SUN:** Methodology, Formal analysis; **Zi-xuan WU:** Formal analysis, Writing − Review & editing; **Liu YANG:** Formal analysis, Writing − Review & editing.

Declaration of competing interest

The authors declare that they have no known competing financial interests or personal relationships that could have appeared to influence the work reported in this paper.

Data Availability statement

The data used to support the findings of this study are available from the corresponding author upon request.

Acknowledgments

This work was supported by Key Laboratory of Infrared Imaging Materials and Detectors, Shanghai Institute of Technical Physics, Chinese Academy of Sciences (No. IIMDKFJJ-21-10) and China Postdoctoral Science Foundation (No. 2018T110993). We would like to thank Analytical and Testing Center of Southwest Jiaotong University (China) for partial testing.

References

[1] YEH J W, CHEN S K, LIN S J, GAN J Y, CHIN T S, SHUN T T, TSAU C H, CHANG S Y. Nanostructured high-entropy alloys with multiple principal elements: Novel alloy design concepts and outcomes [J]. Advanced Engineering Materials, 2004, 6(5): 299−303.

[2] CANTOR B, CHANG I T H, KNIGHT P, VINCENT A J B. Microstructural development in equiatomic multicomponent alloys [J]. Materials Science and Engineering A, 2004, 375/356/377: 213−218.

[3] DU Hu, CAI Jia-hong, WANG Ya-song, YAO Jun-qing, CHEN Qiang, CUI Yu, LIU Xin-wang. Effect of partial recrystallization on microstructure and tensile properties of NiFeCoCrMn high-entropy alloy [J]. Transactions of Nonferrous Metals Society of China, 2022, 32(3): 947−956.

[4] OSMAN H, LIU Lin. Additive manufacturing of high-entropy alloy composites: A review [J]. Transactions of Nonferrous Metals Society of China, 2023, 33(1): 1−24.

[5] SINGH S, WANDERKA N, MURTY B S, GLATZEL U, BANHART J. Decomposition in multi-component AlCoCrCuFeNi high-entropy alloy [J]. Acta Materialia, 2011, 59: 182−190.

[6] HUANG Yuan-sheng, CHEN Ling, LUI Hong-wei, CAI Ming-hong, YEH Jien-wei. Microstructure, hardness, resistivity and thermal stability of sputtered oxide films of $AlCoCrCu_{0.5}NiFe$ high-entropy alloy [J]. Materials Science and Engineering A, 2007, 457: 77−83.

[7] SENKOV O N, SCOTT J M, SENKOVA S V, MIRACLE D B, WOODWARD C F. Microstructure and room temperature properties of a high-entropy TaNbHfZrTi alloy [J]. Journal of Alloys and Compounds, 2011, 509: 6043−6048.

[8] GLUDOVATZ B, HOHENWARTER A, CATOOR D, CHANG E H, GEORGE E P, RITCHIE R O. A fracture-resistant high-entropy alloy for cryogenic applications [J]. Science, 2014, 345(6201): 1153−1158.

[9] STEPANOV N D, YURCHENKO N Y, TIKHONOVSKY M A, SALISHCHEV G A. Effect of carbon content and annealing on structure and hardness of the CoCrFeNiMn-based high entropy alloys [J]. Journal of Alloys and Compounds, 2016, 687: 59−71.

[10] LIU Xiao-qiang, CHENG Hu, LI Zhang-jiang, WANG Hao, CHANG Fa, WANG Wei-guo, TANG Qun-hua, DAI Pin-qiang. Microstructure and mechanical properties of $FeCoCrNiMnTi_{0.1}C_{0.1}$ high-entropy alloy produced by mechanical alloying and vacuum hot pressing sintering [J]. Vacuum, 2019, 165: 297−304.

[11] ZADDACH A J, SCATTERGOOD R O, KOCH C C. Tensile properties of low-stacking fault energy high-entropy alloys [J]. Materials Science and Engineering A, 2015, 636: 373−378.

[12] FERGUSON J B, SHEYKH-JABERI F, KIM C-S, ROHATGI P K, CHO K. On the strength and strain to failure in particle-reinforced magnesium metal-matrix nanocomposites (Mg MMNCs) [J]. Materials Science and Engineering A, 2012, 558: 193−204.

[13] COLOMBINI E, LASSINANTTI GUALTIERI M, ROSA R, TARTERINI F, ZADRA M, CASAGRANDE A, VERONESI P. SPS-assisted Synthesis of SiC_p reinforced high entropy alloys: reactivity of SIC and effects of pre-mechanical alloying and post-annealing treatment [J]. Powder Metallurgy, 2017, 61(1): 64−72.

[14] ROGAL Ł, KALITA D, TARASEK A, BOBROWSKI P, CZERWINSKI F. Effect of SiC nano-particles on microstructure and mechanical properties of the CoCrFeMnNi high entropy alloy [J]. Journal of Alloys and Compounds, 2017, 708: 344−352.

[15] LI Tao, HU Ming-chuan, PEI Xu-hui, DU Yin, ZHOU Wei, WANG Hai-feng. Effect of SiC ceramic nano-particles on microstructure and tribological performance of the AlTiVNbNi refractory high entropy alloy in a wide temperature range [J]. Tribology International, 2024, 198: 109850.

[16] ZHANG Xin-ming, HU Tao, RUFNER J F, LAGRANGE T B, CAMPBELL G H, LAVERNIA E J, SCHOENUNG J M, VAN BENTHEM K. Metal/ceramic interface structures and segregation behavior in aluminum-based composites [J]. Acta Materialia, 2015, 95: 254−263.

[17] JIANG Lin, YANG H, YEE J K, MO Xuan, TOPPING T, LAVERNIA E J, SCHOENUNG J M. Toughening of aluminum matrix nanocomposites via spatial arrays of boron carbide spherical nanoparticles [J]. Acta Materialia, 2016, 103: 128−140.

[18] GUO Lin, GU Ji, DAI Yi-Long, LIN Jian-Guo, SONG Min. Heterogeneous microstructure and mechanical properties of carbon-doped FeCoCrNiMn high-entropy alloy [J]. Transactions of Nonferrous Metals Society of China, 2024, 34(6): 1893−1907.

[19] MENG Ling-long, WANG Xiao-jun, NING Jiang-li, HU Xiao-shi, FAN Guo-hua, WU Kun. Beyond the dimensional limitation in bio-inspired composite: Insertion of carbon nanotubes induced laminated Cu composite and the simultaneously enhanced strength and toughness [J]. Carbon, 2018, 130: 222−232.

[20] CHENG Zhao, ZHOU Hao-fei, LU Qiu-hong, GAO Hua-jian, LU Lei. Extra strengthening and work hardening in gradient nanotwinned metals [J]. Science, 2018, 362(6414): 559−559.

[21] ZHANG Zhi-ming, LI Zan, TAN Zhan-qiu, ZHAO Hai-tao, FAN Gen-lian, XU Yan-jin, XIONG Ding-bang, LI Zhi-qiang. Bioinspired hierarchical Al_2O_3/Al laminated composite fabricated by flake powder metallurgy [J]. Composites Part A: Applied Science and Manufacturing, 2021, 140: 106187.

[22] YIN Z, HANNARD F, BARTHELAT F. Impact-resistant nacre-like transparent materials [J]. Science, 2019,

364(6447): 1260−1263.

[23] GUO Bai-song, SONG Min, ZHANG Xin-ming, CEN Xi, LI Wei, CHEN Biao, WANG Qi-wei. Achieving high combination of strength and ductility of Al matrix composite via in-situ formed Ti−Al_3Ti core−shell particle [J]. Materials Characterization, 2020, 170: 110666.

[24] MA Ji-qiang, FAN Cheng-long, CHEN Wen-yuan, TAN Hui, ZHU Sheng-yu, LI Qing-lin, YANG Jun. Core−shell structure in situ reinforced aluminum matrix composites: Microstructure, mechanical and tribological properties [J]. Journal of Alloys and Compounds, 2022, 901: 163613.

[25] SUN Wan-ting, LUO Jia-si, CHAN Yi-ming, LUAN J H, YANG Xu-sheng. An extraordinary-performance gradient nanostructured Hadfield manganese steel containing multi-phase nanocrystalline-amorphous core−shell surface layer by laser surface processing [J]. Journal of Materials Science & Technology, 2023, 134: 209−222.

[26] LIU Jin-ling, ZHAO Ke, ZHANG Min, WANG Yi-guang, AN Li-nan. High performance heterogeneous magnesium-based nanocomposite [J]. Materials Letters, 2015, 143: 287−289.

[27] LIU Xin-yu, ZHANG Lei, XU Yi. Microstructure and mechanical properties of graphene reinforced $Fe_{50}Mn_{30}Co_{10}$-Cr_{10} high-entropy alloy composites synthesized by MA and SPS [J]. Applied Physics A, 2017, 123(9): 1−7.

[28] LUO Xi, ZHANG Lei-gang, HE Xu, LIU Jin-ling, ZHAO Ke, AN Li-nan. Heterogeneous magnesium matrix nanocomposites with high bending strength and fracture toughness [J]. Journal of Alloys and Compounds, 2021, 855: 157359.

[29] SZKLARZ Z, LEKKI J, BOBROWSKI P, SZKLARZ M B, ROGAL Ł. The effect of SiC nanoparticles addition on the electrochemical response of mechanically alloyed CoCrFeMnNi high entropy alloy [J]. Materials Chemistry and Physics, 2018, 215: 385−392.

[30] PENG Jian, LI Zi-yong, JI Xin-bo, SUN Yan-le, FU Li-ming, SHAN Ai-dang. Decomposition kinetics of carbon-doped FeCoCrNiMn high-entropy alloy at intermediate temperature [J]. Transactions of Nonferrous Metals Society of China, 2020, 30(7): 1884−1894.

[31] PICKERING E J, MUÑOZ-MORENO R, STONE H J, JONES N G. Precipitation in the equiatomic high-entropy alloy CrMnFeCoNi [J]. Scripta Materialia, 2016, 113: 106−109.

[32] HE J Y, ZHU C, ZHOU D Q, LIU W H, NIEH T G, LU Z P. Steady state flow of the FeCoNiCrMn high entropy alloy at elevated temperatures [J]. Intermetallics, 2014, 55: 9−14.

[33] OTTO F, YANG Y, BEI H, GEORGE E P. Relative effects of enthalpy and entropy on the phase stability of equiatomic high-entropy alloys [J]. Acta Materialia, 2013, 61: 2628−2638.

[34] YANG S, ZHANG Y, YAN X, ZHOU H, PI J, ZHU D. Deformation twins and interface characteristics of nano-Al_2O_3 reinforced $Al_{0.4}FeCrCo_{1.5}NiTi_{0.3}$ high entropy alloy composites [J]. Materials Chemistry and Physics, 2018, 210: 240−244.

[35] DENG Y, TASAN C C, PRADEEP K G, SPRINGER H, KOSTKA A, RAABE D. Design of a twinning-induced plasticity high entropy alloy [J]. Acta Materialia, 2015, 94: 124−133.

[36] SHU Rui, JIANG Xiao-song, ZHANG Y.X, WUHRER R, SUN Hong-liang, SHAO Zhen-yi, LUO Zhi-ping. Microstructure and mechanical properties of Mo−Cu−Zr composites fabricated via microwave sintering [J]. Journal of Alloys and Compounds, 2020, 844: 156120.

[37] JIN Xi, ZHOU Yang, ZHANG Lu, DU Xin-yu, LI Bang-sheng. A novel $Fe_{20}Co_{20}Ni_{41}Al_{19}$ eutectic high entropy alloy with excellent tensile properties [J]. Materials Letters, 2018, 216: 144−146.

[38] AKHLAGHI P, AMIRJAN M, PARVIN N. The effect of processing parameters and heat-treatment on the microstructure and mechanical properties of PM $CoCrFeMnNiTi_{0.1}$ high-entropy alloy [J]. Materials Chemistry and Physics, 2021, 257: 123722.

[39] SHEN Lin, ZHAO Yue, LI Yu-lu, WU Hao, ZHU He-guo, XIE Zong-han. Synergistic strengthening of FeCrNiCo high entropy alloys via micro-TiC and nano-SiC particles [J]. Materials Today Communications, 2021, 26: 101729.

[40] ZHOU Jun, LIAO Heng-cheng, CHEN Hao, HUANG Ai-jing. Carbon-alloyed $Fe_{35}Mn_{10}Cr_{20}Ni_{35}$ high entropy alloy synthesized by mechanical alloying plus spark plasma sintering [J]. Journal of Alloys and Compounds, 2021, 859: 157851.

[41] SHUN Tao-tsung, CHANG Liang-yi, SHIU Ming-hua. Microstructure and mechanical properties of multiprincipal component $CoCrFeNiMo_x$ alloys [J]. Materials Characterization, 2012, 70: 63−67.

[42] STEPANOV N D, SHAYSULTANOV D G, SALISHCHEV G A, TIKHONOVSKY M A, OLEYNIK E E, TORTIKA A S, SENKOV O N. Effect of V content on microstructure and mechanical properties of the $CoCrFeMnNiV_x$ high entropy alloys [J]. Journal of Alloys and Compounds, 2015, 628: 170−185.

[43] ZHOU Wei-wei, YAMAMOTO G, FAN Yu-chi, KWON H S, HASHIDA T, KAWASAKI A. In-situ characterization of interfacial shear strength in multi-walled carbon nanotube reinforced aluminum matrix composites [J]. Carbon, 2016, 106: 37−47.

[44] CHEN L B, WEI R, TANG K, ZHANG J, JIANG F, SUN J. Ductile-brittle transition of carbon alloyed $Fe_{40}Mn_{40}Co_{10}Cr_{10}$ high entropy alloys [J]. Materials Letters, 2019, 236: 416−419.

[45] GANJI R S, SAI KARTHIK P, BHANU SANKARA RAO K, RAJULAPATI K V. Strengthening mechanisms in equiatomic ultrafine grained AlCoCrCuFeNi high-entropy alloy studied by micro- and nanoindentation methods [J]. Acta Materialia, 2017, 125: 58−68.

[46] WU Y D, CAI Y H, CHEN X H, WANG T, SI J J, WANG L, WANG Y D, HUI X D. Phase composition and solid solution strengthening effect in TiZrNbMoV high-entropy alloys [J]. Materials & Design, 2015, 83: 651−660.

[47] CHEN Hong-yu, KOSIBA K, LU Ti-wen, YAO Ning, LIU Yang, WANG Yong-gang, PRASHANTH K G, SURYANARAYANA C. Hierarchical microstructures and strengthening mechanisms of nano-TiC reinforced CoCrFeMnNi high-entropy alloy composites prepared by laser powder bed fusion [J]. Journal of Materials Science & Technology, 2023, 136: 245−259.

[48] WU Jian, QIU Huan, ZHU He-guo, XIE Zong-han, CHENG Jia-lin. Influences of Si and C addition on microstructure and mechanical properties of $Fe_{2.5}$CoNiCu high-entropy alloy [J]. Transactions of Nonferrous Metals Society of China, 2023, 33(11): 3406−3417.

[49] SHU Rui, JIANG Xiao-song, LI Jing-rui, SHAO Zhen-yi, ZHU De-gui, SONG Ting-feng, LUO Zhi-ping. Microstructures and mechanical properties of Al−Si alloy nanocomposites hybrid reinforced with nano-carbon and in-situ Al_2O_3 [J]. Journal of Alloys and Compounds, 2019, 800: 150−162.

[50] YE X X, IMAI H, SHEN J H, CHEN B, HAN G Q, UMEDA J, TAKAHASHI M, KONDOH K. Dynamic recrystallization behavior and strengthening-toughening effects in a near-α Ti−xSi alloy processed by hot extrusion [J]. Materials Science and Engineering A, 2017, 684: 165−177.

[51] ZHANG Z, CHEN D. Consideration of Orowan strengthening effect in particulate-reinforced metal matrix nanocomposites: A model for predicting their yield strength [J]. Scripta Materialia, 2006, 54: 1321−1326.

基于新型核壳微结构设计协同增强 CoCrFeNiMn 高熵合金的强度和塑性

刘崇阳[1,2]，蒋小松[1,2]，孙红亮[1,2]，武子轩[3]，杨 刘[4]

1. 西南交通大学 材料先进技术教育部重点实验室，成都 610031；
2. 西南交通大学 材料科学与工程学院，成都 610031；
3. School of Engineering and Materials Science, Queen Mary University of London, London E1 4NS, United Kingdom;
4. Institute for Applied Materials (IAM-WK), Karlsruhe Institute of Technology (KIT), Karlsruhe 76131, Germany

摘 要：通过机械球磨和真空热压烧结(VHPS)成功制备具有新型核壳结构的 SiC@CoCrFeMnNi 高熵合金(HEA)基复合材料(SiC@HEA)。烧结后 SiC@HEA 基复合材料的微观结构由 FCC 固溶体、$Cr_{23}C_6$ 碳化相和 Mn_2SiO_4 氧硅相组成。含有 1.0%(质量分数)SiC 的 SiC@HEA 复合材料的密度和硬度分别为 98.5%和 HV 358.0，抗拉强度为 712.3 MPa，伸长率为 36.2%。核壳结构对裂纹具有显著的偏转作用，这种效应使复合材料有效地保持基体的优异塑性。结果表明，SiC@HEA 复合材料的核壳结构通过多种机制获得优异的强度和塑性。

关键词：高熵合金；SiC 纳米颗粒；微观结构设计；核壳结构；拉伸性能；强塑性协同效应

(Edited by Bing YANG)